AUTHOR	Aye Moe Moe, Rivasto Elmeri, Rijckaert Hannes, Palonen Heikki, Huhtinen Hannu, Van Driessche Isabel, Paturi Petriina
TITLE	Optimized BaZrO3 nanorod density in YBa2Cu3O matrix for high field applications
YEAR	2022, Vol 35(7).
DOI	https://doi.org/10.1088/1361-6668/ac6cac
VERSION	Final draft (AAM) License: CC BY-NC-ND 4.0
CITATION	Aye Moe Moe, Rivasto Elmeri, Rijckaert Hannes, Palonen Heikki, Huhtinen Hannu, Van Driessche Isabel, Paturi Petriina. 2022. Optimized BaZrO3 nanorod density in YBa2Cu3O matrix for high field applications - Superconductor Science and Technology 35 (7). https://doi.org/10.1088/1361-6668/ac6cac

Optimized $BaZrO_3$ nanorod density in $YBa_2Cu_3O_{6+x}$ matrix for high field applications

Moe Moe Aye[1,2], Elmeri Rivasto[1,2], Hannes Rijckaert[3], Heikki Palonen[1], Hannu Huhtinen[1], Isabel Van Driessche[3] and Petriina Paturi[1]

[1] Wihuri Physical Laboratory, Department of Physics and Astronomy, University of Turku, 20014 Turku, Finland

[2] University of Turku Graduate School (UTUGS), University of Turku, 20014 Turku, Finland

[3] SCRiPTS, Department of Chemistry, Ghent University, 9000 Ghent, Belgium

E-mail: `moe.m.aye@utu.fi`

April 2022

Abstract. To maximize the flux pinning in high-temperature superconductor (HTS) thin film applications, we have experimentally studied the effect of $BaZrO_3$ (BZO) nanorod density within the $YBa_2Cu_3O_{6+x}$ (YBCO) lattice. Even though the BZO decreases the self-field critical current density $J_c(0)$ and the absolute $J_c(B)$ at high fields is observed being the highest for 4 % BZO doped YBCO, the maximized pinning property is observed at the level of 10 % of BZO, when the distance between the outer edge of the nanorods is in the order of the diameter of the nanorod. In general, as also theoretically calculated, the flux pinning is increased even above 10 % of BZO, but the improvement is limited by disturbance of the nanorod growth, weakening the flux pinning and decreasing the absolute J_c drastically. The results evidently show that by maximizing the flux pinning using higher BZO doping concentration than earlier expected and taking care of the maximum self-field $J_c(0)$, which is strongly dependent on the electron mean free path, would offer the keys to resolve the challenges in the future HTS power applications.

Keywords: BZO doped YBCO, thin film, HTS superconductors, flux pinning, critical current density

1. Introduction

Among the high temperature superconductors (HTS), the $YBa_2Cu_3O_{6+x}$ (YBCO) thin films and coated conductors have been proved to be optimal and thus promising candidates for the future HTS technological power applications [1, 2, 3, 4]. The material performance and e.g. critical current density in the high magnetic field and wide angular and temperature ranges can be especially improved with artificially produced pinning centers (APCs) which are composed within the YBCO matrix to pin the magnetic flux[5, 6, 7, 3, 8, 9, 10, 11, 12, 13, 14, 15, 16, 17]. However, the optimization of vortex pinning dynamics by maximizing the pinning force [18, 19, 4] is not sufficient enough, since the intrinsic properties of YBCO are doubt when trying to increase the zero field critical current density $J_c(0)$ [18, 4]. To combine these two contributing factors, also the multilayer structures of crystallographically perfect YBCO layers together with optimally APC doped layers have been suggested [9, 14, 20, 1, 21, 22].

So far, the secondary phase perovskite $BaZrO_3$ (BZO) is the most used material to generate nanoscale pinning centers within YBCO lattice by the virtue of its chemical and structural compatibility with YBCO [23, 24, 25]. The BZO nanoinclusions have been proved to be effective APCs that self assemble themselves into energetically preferred nanorod arrays along the YBCO c-axis, leading to significantly enhanced critical current density J_c, especially along the nanorod directions [23, 24, 26, 27, 17, 28, 29]. Therefore, one of the critical issues that needs to be settled is the anisotropy of the flowing current, which in some of the applications is expected to be as constant as possible in all the applied magnetic field directions. Hence, the APC morphology with the mixed alignments of effective pinning centers would indeed provide the formation of strong and isotropic pinning landscape, leading to overall improvement of in-field critical current density $J_c(B)$. For this reason, the numerous approaches for improvements of the highly isotropic angular dependence of J_c by controlling the morphology, dimension, orientation and concentration of APC in the HTS film matrix have been attempted over the past few years [23, 30, 27, 31, 32, 33, 34]. In addition, it has been shown [35, 36, 14, 37, 38, 39] that by controlling the strain field between the film and substrate or between the host material and dopant and, on the other hand, varying the dopant concentration of BZO, the formation of either nanorods along the c-axis or planar nanopatches along the a/b-plane can be tuned. However, the presence of significant strain not only affects the growth of the mixed morphologies of APCs, but it also deteriorates the superconducting performance that can adversely affect flux pinning and thus J_c in YBCO [40, 41, 42, 43]. Therefore, it is still an ongoing challenge to manage the balance between the increased isotropic flux pinning and, on the other hand, the loss of superconductivity, to also approach the depairing current and thus produce the high enough $J_c(0)$ level.

For technological applications, the needed as high as possible $J_c(0)$ can be implemented in different manners. Therefore in this work, we have fully ignored the crystallographically arranged intrinsic YBCO and thus $J_c(0)$ and concentrated only on maximization of the nanorod density to produce the optimized flux pinning at high fields. The effect of nanorod density on J_c is experimentally studied in wide angular range with respect to the external magnetic field and the results are confirmed by molecular dynamics simulations. Finally, the results are profoundly discussed in the light of vortex dynamics theory.

2. Experimental details

A series of superconducting YBCO films with a wide range of BZO (0, 4, 8, 10, 12, and 14 wt%) artificial pinning center concentration, hereafter 0BZO, 4BZO, 8BZO, 10BZO, 12BZO and 14BZO, was grown on single crystalline $SrTiO_3$ (STO) substrates by the pulsed laser deposition (PLD) technique. The target used in the PLD was prepared by the solid state reaction method, the detailed procedure for target preparation is given elsewhere [44]. During the deposition of the films, the optimized deposition parameters were maintained, as presented in our previous work [26]. The x-ray diffraction (XRD) measurements were carried out by Panalytical Empyrean X-ray diffractometer with a 5 axis cradle to characterize the detailed structural properties such as the purity, in-plane and out-of-plane crystalline orientations and lattice strain relaxation of the films. The microstrain in the c-axis direction of the YBCO films was determined following the Williamson–Hall (WH) method on the basis of the integral breadths of the $(00l)$ Bragg reflections [45]. The microstructure of YBCO films were analyzed by employing Cs-corrected JEOL JEM 2200-FS scanning transmission electron microscopy operated at 200 kV with high-angle annular dark-field (HAADF-STEM) detector. Cross-sectional lamellae were prepared by the focused ion beam in an FEI Nova 600 Nanolab Dual Beam scanning electron microscopy and extracted using the *in situ* lift-out procedure with an Omniprobe extraction needle [46]. The YBCO/BZO column ratio was measured and calculated via the image processing software *ImageJ* with the statistical measurement of average spacing of YBCO and diameter of BZO in several cross-sectional areas (high and low resolution images).

Measurements with a Quantum Design Physical Property Measurement System (PPMS) was performed to study the magnetic and resistive properties. The superconducting critical temperatures (T_c) of the films were determined by ac magnetization measurements. By using the Bean critical state model, the critical current densities J_cs were calculated from the opening of the hysteresis loop up to 8 T, as obtained by dc magnetization measurements [47]. The angular and field dependent J_c measurements were performed by a standard four-probe technique. Before the measurement, the standard optical lithographic process was carried out to pattern the 50 μm wide bridges and aluminum wire contacts were made by TPT HB05 Wire Bonder to prepare the electrical connections to the bridges. The angular dependent $J_c(\theta, H, T)$ data were collected in the angular range from 0° to 360° using 3° step with the field range of 1–8 T at temperatures of 10 K and 40 K. The measurements were done at relatively low temperature to avoid the thermal fluctuation effects, especially since T_c is greatly decreased in samples doped with high BZO concentrations.

The angular dependence of the critical current density $J_c(\theta)$ was simulated using molecular dynamics (MD) simulation in order to explain the measured $J_c(\theta)$ curves by modified pinning landscape related to density of BZO nanorods as observed in TEM measurements. Details of the MD simulations were presented elsewhere [48, 28]. To calculate the critical limit of nanorod density, Metropolis simulations were performed

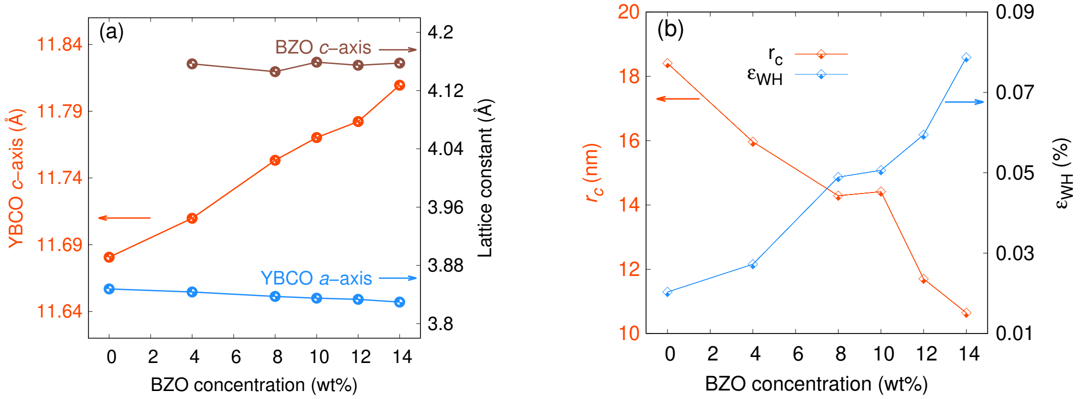

Figure 1. The dopant concentration dependence of c and a lattice parameters (a) and lattice coherent length (r_c) and microstrain (ε_{WH}) calculated by WH method (b) for BZO doped YBCO films.

[49].

3. Results and discussion

3.1. BZO content induced nanorod growth

The structural results characterized by x-ray diffraction θ–2θ and 2D (θ–ϕ) scans show that all the deposited films are epitaxially textured with intense $(00l)$ peaks of YBCO phase and an additional BZO (200) peak at $2\theta \approx 43.3°$. The detailed discussion of XRD results is presented in the supplementary information (SI). As can be seen from the lattice constant dependence on the BZO dopant concentration in Fig. 1(a), the BZO lattice parameter is found to be smaller than the bulk value (4.193 Å), being fairly constant through the whole BZO range. For the YBCO, the c lattice parameter linearly increases with the BZO content and the elongation in 14BZO is obvious. On the other hand, the a/b lattice constant is only slightly decreased with increasing BZO concentration. These facts indicate that the strain induced by the APCs is significantly increased when the BZO concentration is increased within the YBCO matrix. To confirm the produced microstrain in our nanocomposite films, the strain analysis was carried out by the Williamson–Hall method and the results are presented in Fig. 1(b). Clearly, the microstrain is observed to increase with increasing BZO content. Furthermore, the oxygen deficiency, δ, estimated from the intensity ratio of the 2θ (005) and (004) reflections, gives nominal oxygen stoichiometry, i.e. ($0.10 < \delta < 0.13$) [50] (SI), for all the BZO concentrations, indicating that the lengthening of c-axis is not related to oxygen non-stoichiometry. The out-of-plane texture quality determined from the width of FWHM of (005) rocking curve ($\Delta\omega$) also shows the increasing tendency of $\Delta\omega$ with increasing BZO content. The larger $\Delta\omega$ (0.27–0.40 °) values in BZO doped films when compared with the 0BZO (0.23 °) (see SI) is an indication of the enhanced efficiency in the strain generation, when the BZO doping is increased in the films [26, 51]. In

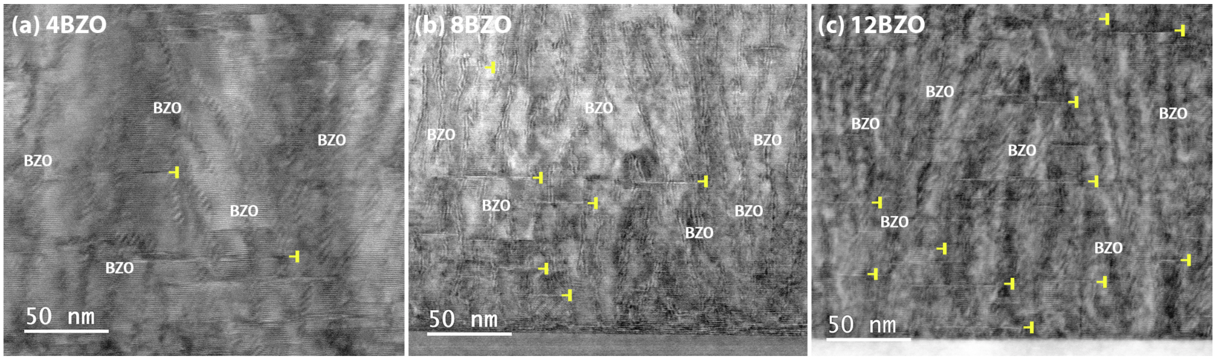

Figure 2. Cross-sectional STEM images of 4 wt.% (a), 8 wt.% (b) and 12 wt.% (c) BZO doped YBCO films. Some of the BZO columns are labeled and the yellow vectors depict stacking faults.

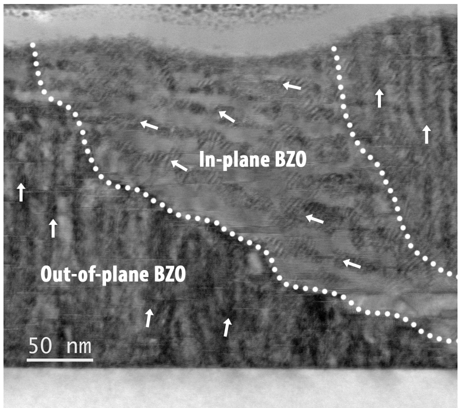

Figure 3. STEM image of 12 wt.% BZO doped YBCO film, indicating that on average 10% of BZO nanorods, usually on the top of the film, are oriented along the in-plane direction of the film. The white arrows show the direction of BZO column.

fact, the coherence length (r_c) along the c-axis linearly decreases with increasing BZO concentration, as can be seen in Fig. 1(b). Hence, in the YBCO/BZO nanocomposite films, the increased strain field produced by the BZO disturbs the YBCO growth, leading to weakened unit cell ordering along the YBCO c-axis.

To get insight into the crystallization behaviour of the BZO doped YBCO films, a scanning transmission electron microscopy (STEM) study is carried out. The cross-sectional STEM images of the 4BZO, 8BZO and 12BZO films are presented in Fig. 2. It is clearly visible that when the BZO content increases, the number of stacking faults (SF) and the volume ratio between BZO columns and YBCO (Table 1) is increased. This is in line with the increased $\Delta\omega$ values (out-of-plane texture) with increasing BZO content. The BZO nanorod diameter and length (shown in Table 2) slightly decrease when BZO content is increased. It also leads to less tilted BZO nanorods and higher BZO nanorod density in the YBCO matrix. The increasing trend of $\Delta\phi$ with increased BZO content indicates that the in-plane texture of YBCO matrix starts to degrade with

Table 1. A compilation of general TEM results such as film thickness, stacking fault (SF) length and distribution, and volumnar ratio between YBCO and BZO columns in 4 wt.% , 8 wt.% and 12 wt.% BZO doped YBCO films.

Films	Film thickness (nm)	SF length (nm)	Remark SF	YBCO/BZO column ratio
4BZO	240 ± 5.5	38.9 ± 13.2	Not whole matrix, often bottom	66%YBCO/34%BZO
8BZO	233 ± 5.5	33.4 ± 14.2	short of ≈ 10 nm (above 150 nm), often with ≈ 35 nm (below 150 nm)	56%YBCO/44%BZO
12BZO	230 ± 6.5	37.2 ± 9.9	often whole film	53%YBCO/47%BZO

Table 2. The parameters of BZO nanorods measured from TEM images for 4 wt.%, 8 wt.% and 12 wt.% BZO doped YBCO films. In 12BZO, approximately 90 % of BZO form YBCO *c*-axis aligned nanorods and 10 % of them are aligned along the *ab*-plane. The splay angles in 12BZO are given from the directions of *c*-axis and *ab*-plane, respectively.

BZO nanorods	Diameter (nm)	Length (nm)	Spacing (nm)	Splay (°)
4BZO	5.9 ± 0.7	49.9 ± 4.7	17.6	16
8BZO	5.5 ± 1.1	32.1 ± 7.9	7.1	14
12BZO(90 % out-of-plane)	5.4 ± 1.0	29.8 ± 15.0	5.6	10
12BZO(10 % in-plane)	9.9 ± 1.3	25.5 ± 5.3	14.5	0-20

higher BZO content (SI). As shown in Fig. 3 and Table 2, in the film grown with the highest BZO content of 12 wt.% (12BZO), approximately 10% of nanorods are aligned along the *ab*-plane and thus only 90% of them are directed along the YBCO *c*-axis. This clearly shows that the absolute maximum for getting maximized nanorod density along the YBCO *c*-axis is around 10 wt.% of BZO in the deposition target.

3.2. Nanorod density governed magnetic properties

Fig. 4(a) presents double-logarithmic plot of J_c as a function of applied magnetic field measured at 10 K for all the deposited films. As can be seen in Figs. 4(a) and 5(b), the self-field $J_c(0)$ is clearly the highest in samples 0BZO and 4BZO, while a dramatic drop between 4BZO and 8BZO can be obtained, having almost a linear decrease in $J_c(0)$ above BZO content of 8%. This is in line with the nanorod density results of APCs, where the BZO dopant induced strain field distorts the YBCO lattice and crystalline quality, by forming dislocations at the interface of BZO and YBCO and decreasing the volume fraction of perfect YBCO [51, 52, 53, 29]. Almost similar but linearly decreasing tendency is observed for T_c within the whole BZO doping range, as can be seen in Fig. 5(a), while the widening of the transition ΔT_c is obvious, especially above the BZO content of 6%.

When looking at the shapes of the $J_c(B)$ curves in Fig. 4(a), we see that the 0BZO exhibits a clear power-law region above the accommodation field with the low-field plateau below it. The value of B^* determined from the relation $J_c(B^*) = 0.9J_c(0)$ [54] for all films are listed in the inset of Fig. 4(a). The maximum B^* value is observed in 4BZO and B^* is decreased with increasing BZO content. When compared with

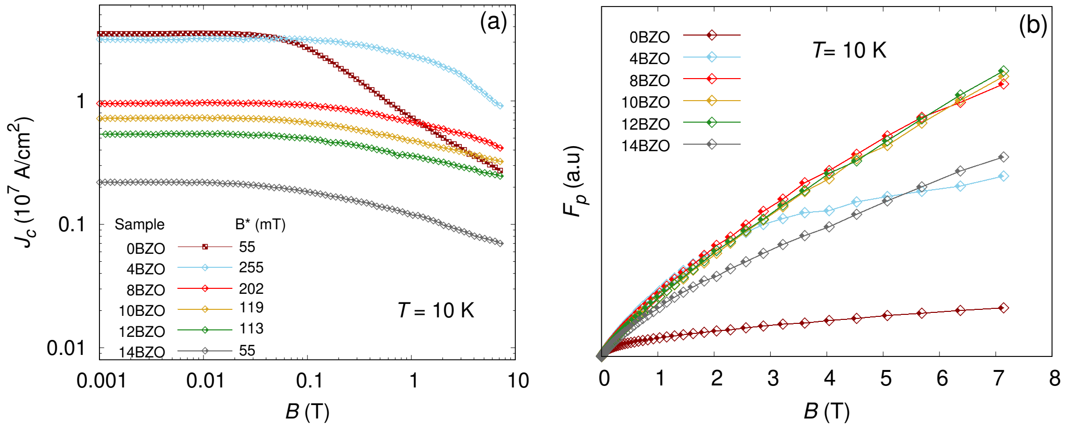

Figure 4. Double-logarithmic plot of the critical current density(J_c) as a function of the applied magnetic field measured at 10 K (a), and magnetic field dependence of the pinning force F_p for BZO doped YBCO films calculated from the normalized J_c values to show the actual differences in terms of pinning. The pinning force is calculated from the relation F_p= J_c*B. The table in (a) shows the accommodation field, B^*, values for BZO doped YBCO films.

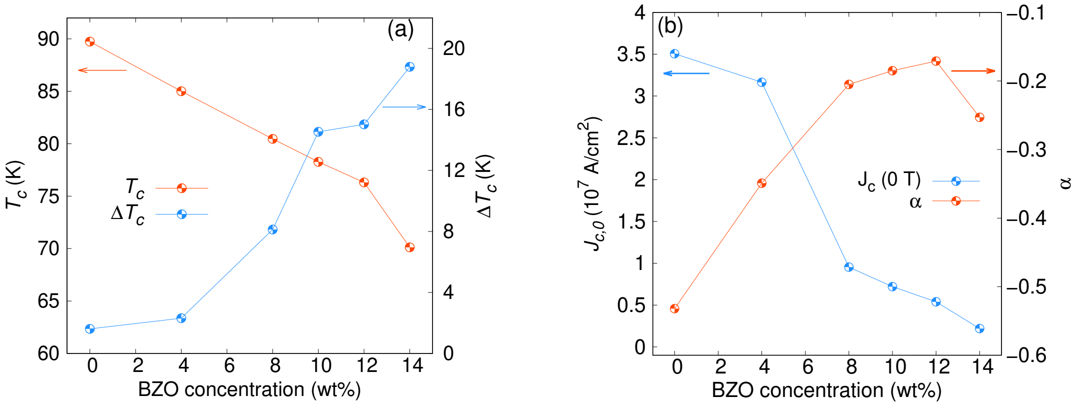

Figure 5. The dopant concentration dependence of the critical temperature T_c and the transition width ΔT_c (a), and the self-field $J_c(0)$ and the power-law fit exponent α (b) for the BZO doped YBCO films.

pristine YBCO, all BZO doped films except 14BZO show higher B^* value and this can be explained by the formation of greater number of individual nanoscale defects. Moreover, the matching field (B_ϕ) values estimated from nanorod spacings of the TEM images are ≈ 7 T for 4BZO, ≈ 41 T for 8BZO and ≈ 66 T for 12BZO. When introducing the 1D nanocolumnar defects into the YBCO matrix, the shape of the $J_c(B)$ curve changes dramatically, having similar type of pinning behaviour from 4BZO to 14BZO samples. In the presence of applied magnetic field, the 4BZO shows unambiguously the highest J_c in the whole applied magnetic field range and a clear decreasing tendency in the in-field J_c with increasing BZO dopant concentration can be seen in Fig. 4(a).

However, the decrease of J_c in high magnetic field range seems to be associated with the matching field linked BZO nanorod density, since the drop of J_c in the 4BZO is observed to be faster at fields above 3 T, while in samples 8BZO, 10BZO and 12BZO reduction with increasing field is clearly smaller.

To examine the pinning strength in the YBCO films with different BZO nanorod densities, the pinning force (F_p) is calculated from the normalized J_c as a function of magnetic field measured at 10 K (Fig. 4(b)). It is worth noting that the pinning performance of 8BZO, 10BZO and 12BZO is clearly stronger in comparison with 4BZO in the magnetic fields above 2.5 T. The similar behaviour with maximized pinning property around 10% BZO doping can be obtained in Fig. 5(b), where the exponent α in the $J_c(B)$ power-law region increases rapidly up to the BZO concentration of 8%, being almost constant until the formation BZO nanorods transforms their shape, as discussed earlier in the section of growth mechanisms.

The magnetic results clearly indicate the effectiveness of the nanocolumnar defects in the YBCO matrix, which evidently provide enhanced correlated pinning along the applied magnetic field up to the maximum nanorod density with $\approx 10\,\%$BZO until the formation of other types of defects starts to be too powerful.

3.3. Field dependent critical current density

The resistively measured critical current anisotropy curves $J_c(\theta)$ under 0.5–8 T applied fields are presented in Fig. 6(a-d). One can observe substantial variation between the shapes of the measured $J_c(\theta)$ curves, such as evolution of the *c*- and *ab*-peaks as the field is increased. In the case of 0BZO, the characteristic anisotropy of YBCO can be observed. When comparing the $J_c(\theta)$ curves of the doped samples to 0BZO, one can observe remarkable differences resulting from the vortex pinning limited J_c. In particular, the differences in the evolution of the increased J_c near $\theta = 0^\circ$ and $\theta = 90^\circ$, that are the *c*- and the *ab*-peaks, respectively, suggest major differences in the pinning mechanisms between the differently doped samples. Recalling the previously discussed results of the TEM images, only the 4–10% BZO doped samples have well defined *c*-axis oriented nanorods, while for the 12% and 14% the pinning structure becomes more complicated as regions of *ab*-oriented BZO start to appear. This may be a reason why the measured $J_c(\theta)$ curves for 12BZO and 14BZO resemble the characteristic anisotropy obtained for the 0BZO. Notice, that absolute value of the J_c for the 12BZO and the 14BZO are also remarkably lower when compared with other samples over the whole angular range.

We focus the discussion related to the shapes of the $J_c(\theta)$ curves to 4–10% doped samples, for which clear *c*-axis oriented nanorods were observed. We try to undestand the observed differences by considering a simple model based on the vortex paths [55]. We argue that the $J_c(\theta)$ is directly proportional to the product of the associated pinning strength and the probability of a vortex meeting a pinning center. The pinning strength is maximized when $\theta = 0^\circ$ or $\theta = 90^\circ$, where former results from the vortices

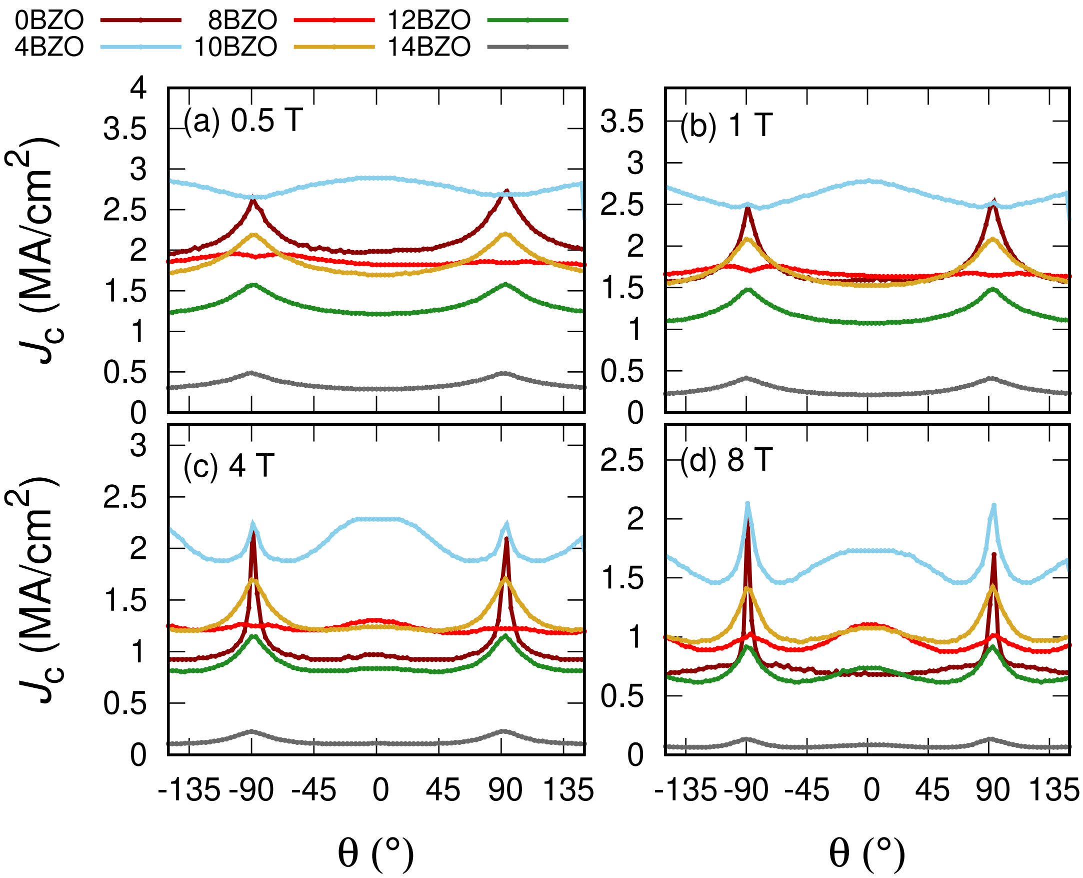

Figure 6. The resistively measured critical current anisotropies for samples with varying BZO concentration at 40 K under applied fields of (a) 0.5 T (b) 1 T (c) 4 T and (d) 8 T. The $\theta = 0°$ corresponds to the direction along the *c*-axis of the YBCO unit cell.

aligning themselves parallel to the nanorods, while the latter is because of increased multicolumn pinning. The strength of the multicolumn pinning, in particular, is inversely proportional to the substantially varying spacing of the nanorods between the differently doped samples. Moreover, the probability of vortex meeting a pinning site intuitively increases as a function of θ. In the high field range near $\theta = 0°$ and $\theta = 90°$, where the pinning strength is maximized, it is possible that the vortices get stabilized outside the nanorods via the repulsive vortex-vortex interactions [28]. This seemingly increases the pinning efficiency and manifests as more pronounced *c*- and *ab*-peaks in the high field range. The interplay of the above mentioned processes can intuitively explain the shapes of the $J_c(\theta)$ curves of differently doped samples.

In the case of the 4BZO doped sample, the *c*-peak is present in all of the measured magnetic fields, while the *ab*-peak slightly emerges around 1 T and increases as a function of field up to 8 T. As the *ab*-peak is completely absent at 0.5 T, we conclude that the J_c is limited by the vortex pinning on the full angular range. The absence of the *ab*-peak in the low field range can be explained by the large spacing of the nanorods (17.6 nm) as obtained from the TEM images. As mentioned above, the spacing of the nanorods is inversely proportional to the strength of the multicolumn pinning for high θ. In the case of 4BZO, the multicolumn pinning is negligible and the c-axis pinning dominates the J_c even for high θ values. The ab-peak rises as the magnetic field is increased due to increasing vortex-vortex interactions which magnify the pinning probability for high θ.

For the 8BZO, the $J_c(\theta)$ is extremely flat in the low field range, while the c- and ab-peaks start to slowly emerge as the field is increased up to 4 T. The flat $J_c(\theta)$ curve at the low field range can be explained by the particular nanorod spacing (7.1 nm), for which the strength of the multicolumn pinning is comparable to the single column pinning in the full angular range. The slightly reduced pinning force for high θ is compensated by the increased pinning probability. In the high field range, the vortex-vortex interactions start to enhance the pinning efficiency in particular for θs where the strongest pinning occurs, that are near c- and ab-directions. Thus, the c- and ab-peak emerge in the high field range.

Finally, in the case of the 10BZO, the ab-peak can be observed to be present in the full magnetic field range, while the c-peak emerges only at the high field range. In this case, the nanorod spacing is smaller when compared with the 8BZO and we can expect substantially increased pinning efficiency as θ is increased due to increased multicolumn pinning and pinning probability. Again, the c- and the ab-peaks emerge in the high field range as the vortex-vortex interactions remarkably increase the pinning probability along these directions.

The highest absolute value of the J_c is obtained for 4BZO in all of the measured magnetic fields. This is due to optimal BZO concentration which balances the reduced $J_c(B = 0)$ with the good vortex pinning performance. However, based on the analysis of the $J_c(\theta)$ curves, the 4BZO does not seem to have the best pinning performance despite the transcendent J_c. The optimization of the density of the nanorod lattice in terms of the pinning performance is discussed in the following section.

4. Optimizing the flux pinning by increased nanorod density

In order to support the obtained experimental results, according to which approximately 10% BZO concentration produces the maximal flux pinning and thus optimal BZO nanorod density, we have theoretically studied the relation between the vortex dynamics limited J_c and nanorod density. We express the nanorod density via a more useful quantity, that is the nanorod spacing (s) illustrated in Fig. 7(a). The simplest way to study the s dependence of J_c is to calculate 1-dimensional vortex potential energy distribution for a system of $N_{\mathrm{nr}} = 2$ nanorods of radius R separated by various s. We have done this for nanorods of radius $R = 3$ nm, corresponding to BZO, using the widely

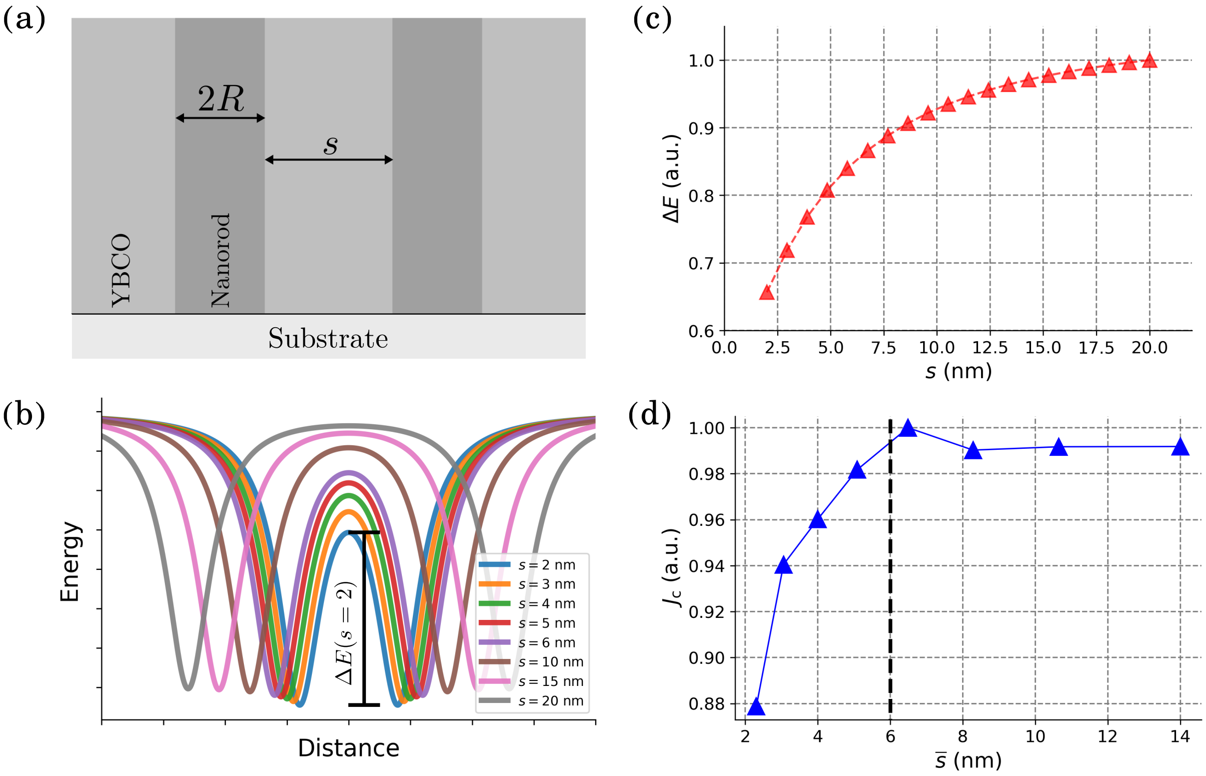

Figure 7. (a) A schematic illustration of nanorods within the superconducting lattice along with the defined length measures. (b) The 1-dimensional potential experienced by a single vortex created by two nanorods of radius $R = 3\,\mathrm{nm}$ separated by distance s. (c) The vortex hopping potential as a function of the nanorod separation calculated from similar potential curves that is presented in (b). (d) The results of the Metropolis simulations. The data points represent obtained minimum values of 30 statistical repetitions for specific $\overline{s}$. The dashed line represents the critical distance of $2R = 6\,\mathrm{nm}$.

used pinning potential [18]

$$\epsilon_{\mathrm{vp}}(\mathbf{r}) = -\frac{\epsilon_0}{2}\sum_{i=0}^{N_{\mathrm{nr}}}\frac{R_i^2}{|\mathbf{r}_i - \mathbf{r}|^2 + 2\xi^2}, \tag{1}$$

where the index i labels the nanorod, $\epsilon_0 = \Phi_0^2/(4\pi\mu_0\lambda^2)$ is an energy constant and λ and ξ are the magnetic penetration depth and coherence length along the ab-plane of YBCO, respectively. The results are presented in Fig. 7(b), where one can clearly observe a drastic decrease in the vortex hopping potential (ΔE) as s is decreased. The corresponding ΔEs as a function of s are presented in Fig. 7(c). As the $J_c \sim \exp(\Delta E/kT)$, where k is the Boltzmann constant and T is the temperature, the obtained $\Delta E(s)$ curve suggests a rapid decrease of J_c as the s is decreased.

In order to demonstrate this more profoundly, we have performed Metropolis-Hastings method based vortex dynamics simulations in a 2-dimensional $A = 100 \times 100\,\mathrm{nm}^2$ grid oriented parallel to the ab-plane of YBCO, along which periodic boundary conditions are applied. The system was first initialized by placing a desired number of

N_{nr} nanorods of radius $R = 3\,\mathrm{nm}$ within the grid. The number of nanorods is related to the average nanorod separation ($\overline{s}$) by a formula $\overline{s} = \sqrt{A/N_{\mathrm{nr}}} - 2R$. After this, a number of $N_{\mathrm{v}} = BA/\Phi_0$ YBCO c-axis oriented vortices, where Φ_0 is the magnetic flux quantum and $B = 1\,\mathrm{T}$, were placed one by one at the calculated energy minimum positions of the grid. This requires the calculation of the vortex potential energy distribution over the grid which was done by evaluating the pinning potential at position $\mathbf{r}$ using Eq. (1). Moreover, we have also taken into account the vortex-vortex interactions using the formula [18]

$$\epsilon_{\mathrm{vv}}(\mathbf{r}) = \sum_{i=0}^{N_{\mathrm{v}}} \epsilon_0 t_{\mathrm{f}} \begin{cases} \mathrm{K}_0\left(\frac{|\mathbf{r}_i - \mathbf{r}|}{\lambda(T)}\right), & \text{when } |\mathbf{r}_i - \mathbf{r}| > \xi \\ 2 \cdot \mathrm{K}_0\left(\frac{\xi(T)}{\lambda(T)}\right), & \text{when } |\mathbf{r}_i - \mathbf{r}| \leqslant \xi \,, \end{cases} \tag{2}$$

where the index i labels the already placed vortices and K_0 is the zeroth order modified Bessel function. Finally, the applied potential manifesting as the current density J through the superconductor was taken into account by a simple relation

$$\epsilon_{\mathrm{appl}} \sim Jx, \tag{3}$$

where x is the position of the vortex along the x-direction of the grid. The total potential at position $\mathbf{r}$ thus becomes the sum of Eqs. (1)–(3).

Once the initial state has been created, the system was evolved using the Metropolis-Hastings algorithm [49], that is by iterating the following set of rules: i) Calculate the total energy of the system in the *initial state* (E_0). ii) Create *excited state* by changing the position of randomly chosen vortex in random direction by Δr. iii) Calculate the new total energy of the system after the displacement (E_1). iv) If $E_1 < E_0$, accept the *excited state* to be the new *initial state* of the system. Else, accept the *excited state* with probability of $p = \exp(-\Delta E/kT)$, where $\Delta E = E_1 - E_0$.

In this work, we set $\Delta r = 0.037\,\mathrm{nm}$, so that the acceptance probability for $J = 0$ was around 10% and increases up to ~50% for currents in the range of the obtained J_{c}s at $T = 10\,\mathrm{K}$. The J_{c} was determined using the bisection method as the J, for which the average position of the vortices changes more than R over $N_{\mathrm{v}} \cdot 500$ iterations. The simulations for a single $J_{\mathrm{c}}(\overline{s})$ were repeated for 30 times, from which the lowest obtained value was determined as the final $J_{\mathrm{c}}(\overline{s})$ presented in Fig. 7(d). The J_{c} can be observed to decay rapidly from a somewhat constant value once $\overline{s} < 2R$. This suggests that there exists an universal critical nanorod density corresponding to $\overline{s} = 2R$, above which the vortex dynamics limited J_{c} is decreased due to the reduced hopping potential between the adjacent nanorods. This result is perfectly in line with the experimental observations presented in previous sections.

Increasing the nanorod concentration up the critical limit is typically observed to increase the vortex dynamics limited J_{c} accordingly. This effect, however, is absent in the simulated $J_{\mathrm{c}}(\overline{s})$ curve presented in Fig. 7(c), where the J_{c} appears to be somewhat constant for $\overline{s} > 2R$. This is, however, expected as the increase of J_{c} for this region is due to increased probability of a vortex coming across a pinning site (p). Explicitly, one can write $J_{\mathrm{c}} \sim p$ and $p \sim \overline{s}$. The p does not have an effect in our simulation, as the

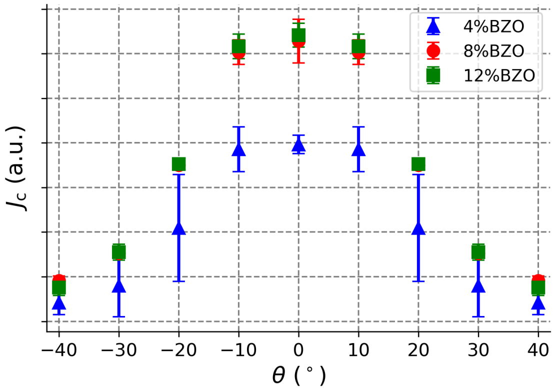

Figure 8. The simulated c-peaks for various BZO doping concentrations using the MD based vortex dynamics model presented in [48] and SI.

system was initialized by placing the vortices into the minimum energy positions of the grid in the first place. However, we have demonstrated this effect by running molecular dynamics (MD) method based vortex dynamics simulations using the model presented in [48] and SI. This simulation model allows the simulation of the J_c anisotropy in the vicinity of the YBCO c-axis and takes also into account the pinning probability p. The MD simulations were performed in a $150 \times 150\,\mathrm{nm}^2$ grid using 10 adjacent layers with pinning structures consisting of varying number of YBCO c-axis oriented nanorods, the number of which is calculated from the desired concentration (σ) using the formula $\sigma = N_{\mathrm{nr}}\pi R^2/(A - N_{\mathrm{nr}}\pi R^2)$, where A is the area of the associated grid along the YBCO ab-plane. The c-peak under $1\,\mathrm{T}$ applied field was simulated for 4%, 8% and 12% BZO doped samples and the results are presented in Fig. 8. The critical current can be observed to increase as the nanorod concentration is increased up to 12%, corresponding to the critical nanorod density. This is, in particular, due to the increasing p as a function of the number of nanorods below the critical limit. Again, we want to point out that as the dopant concentration dependency of the $J_c(B = 0)$ has not been taken into account, the simulated J_cs are purely related to the vortex pinning performance of the associated grid. These results are fully in line with our experimental observations, where the maximal pinning was observed for pinning structures for which the distance between the outer edges of the nanorods is roughly equal to the nanorod diameter.

In summary, we have theoretically proven that the vortex pinning limited J_c obtains the highest value in a pinning structure where the nanorods of radius R are separated by a distance $s \approx 2R$.

5. Conclusions

In this work, we have varied the BZO concentration within the YBCO matrix to manufacture the optimal nanorod density, which again could produce the maximal flux pinning for high field applications. Although the flux pinning increases as a function of nanorod density, we observed the maximum BZO concentration of approximately 10%, above which the growth mechanism is strongly modified, turning the *c*-axis oriented BZO nanorods growing along the *ab*-plane thus reducing the effective pinning force dramatically. Based on our experimental results and theoretical simulations, in reality the maximal flux pinning is reached when the nanorod density is such that the distance between the nanorods is approximately the same as the diameter of the nanorod. This result clearly gives a hint that improving the crystalline quality of the YBCO film for example forming multilayer structures with layers having the optimal electron mean free path, higher BZO concentration can be used in some other layers for getting the best possible combined effect for reaching superior critical current density for desired HTS power applications.

6. Acknowledgements

The Jenny and Antti Wihuri Foundation and the University of Turku Graduate School are acknowledged for financial support. Hannes Rijckaert acknowledges support and funding as postdoctoral fellow fundamental research of the Research Foundation-Flanders (FWO, Grant number 1273621N).

References

[1] Foltyn S R, Civale L, MacManus-Driscoll J L, Jia Q X, Maiorov B, Wang H and Maley M 2007 *Nat. Mater.* **6** 631–642

[2] Holesinger T G, Civale L, Maiorov B, Feldmann D M, Coulter J Y, Miller D J, Maroni V A, Chen Z, Larbalestier D C, Feenstra R, Li X, Huang Y, Kodenkandath T, Zhang W, Rupich M W and Malozemoff A P 2008 *Adv. Mater.* **20** 391–407

[3] Matsumoto K and Mele P 2010 *Supercond. Sci. Technol.* **23** 014001:1–12

[4] Obradors X and Puig T 2014 *Supercond. Sci. Technol.* **27** 044003:1–17

[5] Larbalestier D, Gurevich A, Feldmann D M and Polyanskii A 2001 *Nature* **414** 368–377

[6] Civale L, Maiorov B, Serquis A, Willis J O, Coulter J Y, Wang H, Jia Q X, Arendt P N, MacManus-Driscoll J L, Maley M P and Foltyn S R 2004 *Appl. Phys. Lett.* **84** 2121–2123

[7] Kang S, Goyal A, Li J, Gapud A A, Martin P M, Heatherly L, Thompson J R, Christen D K, List F A, Paranthaman M and Lee D F 2006 *Science* **311** 1911–1914

[8] Goyal A, Kang S, Leonard K J, Martin P M, Gapud A A, Varela M, Paranthaman M, Ijadoula A O, Specht E D, Thompson J R, Christen D K, Pennycook S J and List F A 2005 *Supercond. Sci. Technol.* **18** 1533–1538

[9] Maiorov B, Baily S A, Zhou H, Ugurlu O, Kennison J A, Dowden P C, Holesinger T G, Foltyn S R and Civale L 2009 *Nat. Mater.* **8** 398–404

[10] Baca F J, Haugan T J, Barnes P N, Holesinger T G, Maiorov B, Lu R, Wang X, Reichart J N and Wu J Z 2013 *Adv. Funct. Mater.* **23** 4826–4831

[11] Jha A K, Matsumoto K, Horide T, Saini S, Mele P, Ichinose A, Yoshida Y and Awaji S 2016 *IEEE T. Appl. Supercond.* **26** 8000404:1–4

[12] Blatter G, Geshkenbein V B and Koopmann J A G 2004 *Phys. Rev. Lett.* **92** 067009

[13] Wee S H, Goyal A, Zuev Y L and Cantoni C 2008 *Supercond. Sci. Technol.* **21** 092001:1–4

[14] Wu J Z, nd F J Baca J J S, Emergo R, Wilt J and Haugan T J 2015 *Supercond. Sci. Technol.* **28** 125009

[15] Gutiérrez J, Puig T and Obradors X 2007 *Appl. Phys. Lett.* **90** 162514:1–3

[16] Gutiérrez J, Llordés A, Gázquez J, Gibert M, Romà N, Ricart S, Pomar A, Sandiumenge F, Mestres N, Puig T and Obradors X 2007 *Nat. Mater.* **6** 367–373

[17] Khan M Z, Rivasto E, Tikkanen J, Rijckaert H, Malmivirta M, Liedke M O, Butterling M, Wagner A, Huhtinen H, Driessche I V and Paturi P 2019 *Sci. Reports* **9** 15425:1–12

[18] Blatter G, Feigel'man M V, Geshkenbein V B, Larkin A I and Vinokur V M 1994 *Reviews of Modern Physics* **66** 1125–1388

[19] Matsushita T 2007 *Flux pinning in superconductors* (Springer, Heidelberg, Germany)

[20] Horide T, Kawamura T, Matsumoto K, Ichinose A, Yoshizumi M, Izumi T and Shiohara Y 2013 *Supercond. Sci. Technol.* **26** 075019

[21] Haugan T, Barnes P N, Wheeler R, Meisenkothen F and Sumption M 2004 *Nature* **430** 867

[22] Barnes P N, Haugan T J, Varanasi C V and Campbell T A 2004 *Appl. Phys. Lett.* **85** 4088

[23] MacManus-Driscoll J L, Foltyn S R, Jia Q X, Wang H, Serquis A, Civale L, Maiorov B, Hawley M E, Maley M P and Peterson D E 2004 *Nat. Mater.* **3** 439–443

[24] Wang X, Baca F J, Emergo R L S, Wu J Z, Haugan T J and Barnes P N 2010 *J. Appl. Phys.* **108** 113911

[25] Augieri A, Celentano G, Galluzzi V, Mancini A, Rufoloni A, Vannozzi A, Armenio A A, Petrisor T, Ciontea L, Rubanov S, Silva E and Pompeo N 2010 *J. Appl. Phys.* **108** 063906

[26] Peurla M, Paturi P, Stepanov Y P, Huhtinen H, Tse Y Y, Bódi A C, Raittila J and Laiho R 2006 *Supercond. Sci. Technol.* **19** 767–771

[27] Mele P, Matsumoto K, Ichinose A, Kukaida M, Yoshida Y, Horii S and Kita R 2008 *Supercond. Sci. Technol.* **21** 125017

[28] Rivasto E, Khan M Z, Malmivirta M, Rijckaert H, Aye M M, Hynninen T, Huhtinen H, Driessche I V and Paturi P 2020 *Sci. Reports* **10** 3169:1–14

[29] Aye M M, Khan M Z, Rivasto E, Tikkanen J, Huhtinen H and Paturi P 2019 *IEEE T. Appl. Supercond.* **29** 8000805

[30] Gapud A A, Kumar D, Viswanathan S K, Cantoni C, Varela M, Abiade J, Pennycook S J and Christen D K 2005 *Supercond. Sci. Technol.* **18** 1502

[31] Varanasi C V, Barnes P N and Burke J 2007 *Supercond. Sci. Technol.* **20** 1071

[32] Goyal A, Kang S, Leonard K J, Martin P M, Gapud A A, Varela M, Paranthaman M, Ijaduola A O, Specht E D, Thompson J R, Christen D K, Pennycook S J and List F A 2005 *Supercond. Sci. Technol.* **18** 1533

[33] Xu A, Jaroszynski J, Kametani F and Larbalestier D 2015 *Appl. Phys. Lett.* **106** 052603

[34] Haugan T, Barnes P N, Wheeler R, Meisenkothen F and Sumption M 2004 *Nature (London)* **430** 867

[35] Baca F J, Barnes P N, Emergo R L S, Haugan T J, Reichart J N and Wu J Z 2009 *Appl. Phys. Lett.* **94** 102512

[36] Yang H, Wang H, Maiorov B, Lee J, Talbayev D, Hinton M J, Feldmann D M, MacManus-Driscoll J L, Taylor A J, Civale L and Lemberger T R 2009 *J. Appl. Phys.* **106** 093914:1–4

[37] Wu J, Shi J, Baca J, Emergo R, Elliot A, Wilt J, Sebastian M A, Haugan T and Varanasi C V 2015 *IEEE T. Appl. Supercond.* **25** 8000205:1–5

[38] Zhao R, Li W, Lee J H, Choi E M, Liang Y, Zhang W, Tang R, Wang H, Jia Q, MacManus-Driscoll J L and Yang H 2014 *Adv. Funct. Mater.* **24** 5240–5245

[39] Wu J and Shi J 2017 *Supercond. Sci. Technol.* **30** 103002

[40] Foltyn S R, Civale L, MacManus-Driscoll J L, Jia Q X, Maiorov B, Wang H and Maley M 2007 *Nat. Mater.* **6** 631

[41] Ichinose A, Naoe K, Horide T, Matsumoto K, Kita R, Mukaida M, Yoshida Y and Horii S 2007 *Supercond. Sci. Technol.* **20** 1144–1150

[42] Mele P, Matsumoto K, Horide T, Ichinose A, Mukaida M, Yoshida Y, Horii S and Kita R 2008 *Supercond. Sci. Technol.* **21** 032002

[43] Cantoni C, Gao Y, Wee S H, Specht E D, Gazquez J, Meng J, Pennycook S J and Goyal A 2011

ACS Nano **5** 4783–4789

[44] Raittila J, Huhtinen H, Paturi P and Stepanov Y P 2002 *Physica C* **371** 90–96

[45] Birkholz M 2006 *Thin Film Analysis by X-ray Scattering* (Wiley-VCH)

[46] Rijckaert H, Pollefeyt G, Sieger M, Hänisch J, Bennewitz J, Keukeleere K D, Roo J D, Hühne R, Bäcker M, Paturi P, Huhtinen H, Hemgesberg M and Driessche I V 2017 *Chemistry of Materials* **29** 6104–6113

[47] Wiesinger H P, Sauerzopf F M and Weber H W 1992 *Physica C* **203** 121–128

[48] Paturi P, Malmivirta M, Hynninen T and Huhtinen H 2018 *J. Phys. Cond. Mat.* **30** 315902:1–7

[49] Metropolis N, Rosenbluth A W, Rosenbluth M N, Teller A H and Teller E 1953 *J. Chem. Phys.* **21** 1087–1092

[50] Ye J and Nakamura K 1993 *Phys. Rev. B* **48** 7554–7564

[51] Peurla M, Huhtinen H, Tse Y Y, Raittila J and Paturi P 2007 *IEEE T. Appl. Supercond.* **17** 3608–3611

[52] Kang S, Goyal A, Li J, Martin P, Ijaduola A, Thompson J R and Paranthaman M 2007 *Physica C* **457** 41

[53] Haugan T J, Barnes P N, Campbell T A, Pierce N A, Baca F J and Maartense I 2007 *IEEE T. Appl. Supercond.* **17** 3724

[54] Cai C, Holzapfel B, Hänisch J, Fernandez L and Schultz L 2004 *Phys. Rev. B* **69** 104531

[55] Long N J 2008 *Supercond. Sci. Technol.* **21** 025007:1–8